

Обзор ArXiv: astro-ph,
21-31 января 2019 года

От Сильченко О.К.

ArXiv: 1901.09123

Kinematics of Circumgalactic Gas: Feeding Galaxies and Feedback

CRYSTAL L. MARTIN¹

STEPHANIE H. HO¹

GLENN G. KACPRZAK²

CHRISTOPHER W. CHURCHILL³

¹*Department of Physics, University of California, Santa Barbara, Santa Barbara, CA 93106, USA*

²*Center for Astrophysics and Supercomputing, Swinburne University of Technology, Hawthorn, Victoria 3122, Australia*

³*Department of Astronomy, New Mexico State University, Las Cruces, NM 88003, USA*

(Received January 31, 2019)

ABSTRACT

We present observations of 50 pairs of redshift $z \approx 0.2$ star-forming galaxies and background quasars. These sightlines probe the circumgalactic medium (CGM) out to half the virial radius, and we describe the circumgalactic gas kinematics relative to the reference frame defined by the galactic disks. We detect halo gas in Mg II absorption, measure the equivalent-width-weighted Doppler shifts relative to each galaxy, and find that the CGM has a component of angular momentum that is aligned with the galactic disk. No net counter-rotation of the CGM is detected within 45° of the major axis at any impact parameter. The velocity offset of the circumgalactic gas correlates with the projected rotation speed in the disk plane out to disk radii of roughly 70 kpc. We confirm previous claims that the Mg II absorption becomes stronger near the galactic minor axis and show that the equivalent width correlates with the velocity range of the absorption. We cannot directly measure the location of any absorber along the sightline, but we explore the hypothesis that individual velocity components can be associated with gas orbiting in the disk plane or flowing radially outward in a conical outflow. We conclude that

Выборка: 50 пар галактика-квазар

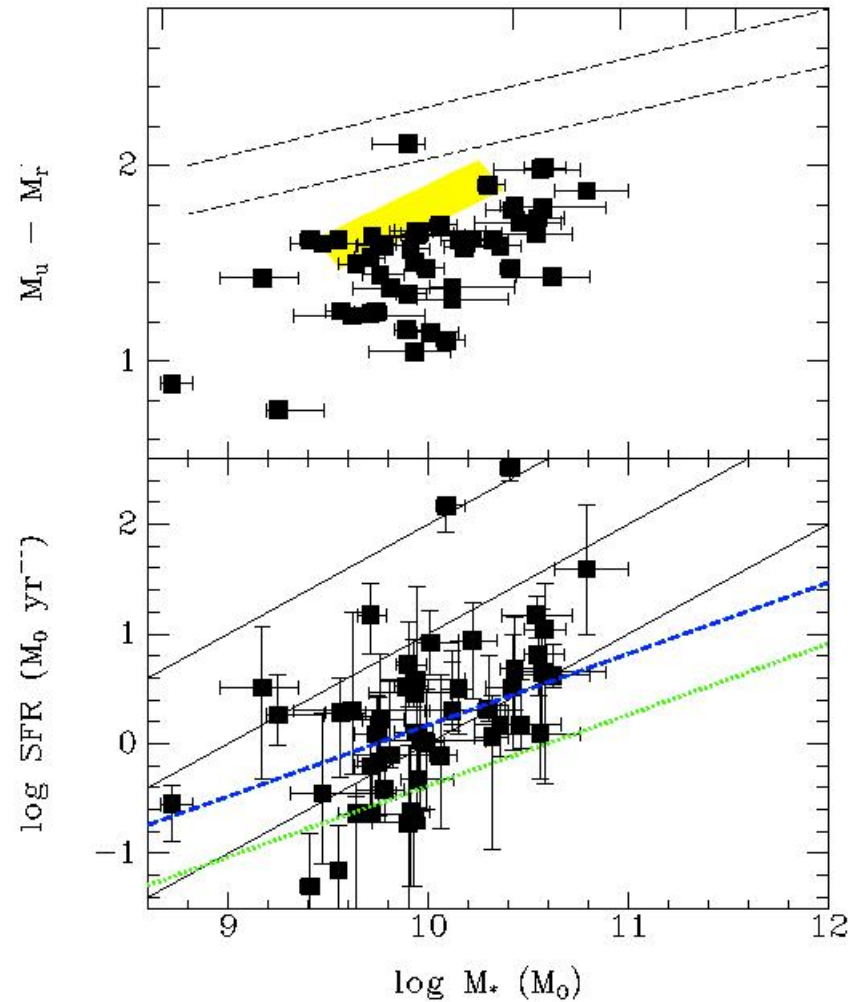
the sample to $z > 0.15$ galaxies in order to redshift the Mg II $\lambda\lambda 2796, 2803$ doublet longward of the atmospheric limit. We also chose low redshift galaxies because we wanted to spatially resolve morphological features.

These star-forming galaxies have a median redshift of $z \approx 0.21$ so they are fainter than the Sloan Digital Sky Survey DR9 (SDSS, Ahn et al. (2012)) spectroscopic sample. We used photometric redshifts to select the galaxies but then measured spectroscopic redshifts from our new spectra. These redshift revisions mean that our selection criteria are not strict limits.

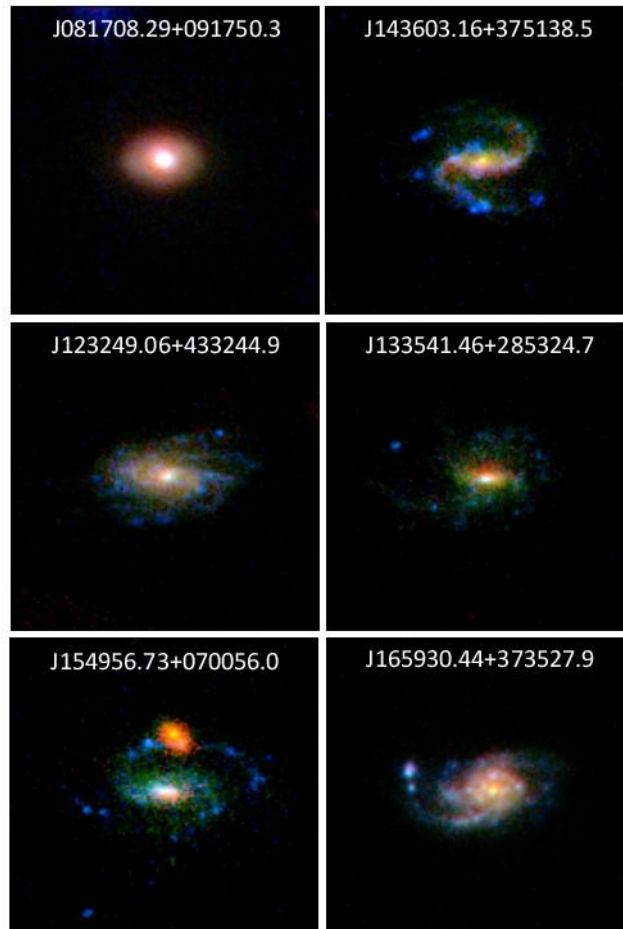
Passive, red galaxies were excluded from the galaxy sample using a color cut $M_u - M_r < 2.0$ (Schawinski et al. 2014). We rejected galaxies with disks observed face-on by requiring the SDSS r -band semi-minor axis to be less than 0.71 times the length of the semi-major axis. We later obtained higher resolution imaging and revised the disk inclination and position angle measurements for a few galaxies.

Our target galaxies are the subset of this sample with a background quasar brighter than $u = 18.5$ and impact parameters $b < 100$ kpc, corresponding to 10-50% of the halo virial radius. We inspected the SDSS DR9 spectra of these quasars, eliminating a few Lyman-limit systems and misidentified stars, and obtained a parent sample of galaxy – quasar pairs. Our observational campaign prioritized pairs with $b < 60$ kpc.

Характеристики выборки



Примеры



Диапазон прицельных параметров

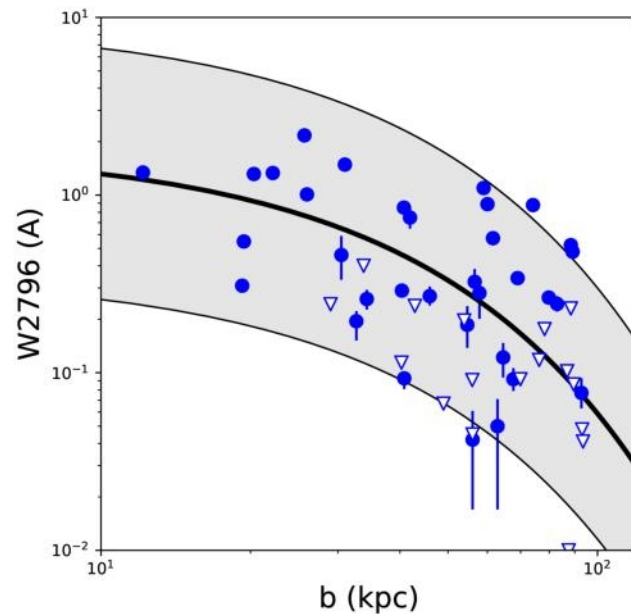


Figure 6. Rest-frame equivalent width of Mg II 2796 versus impact parameter. Absorption strength declines with the distance of the sightline from the galaxy, consistent with previous studies. For comparison, the black line shows the maximum likelihood fit from Nielsen et al. (2013); the shaded region shows the root-mean-square variation between this fit and their sample.

Распределение

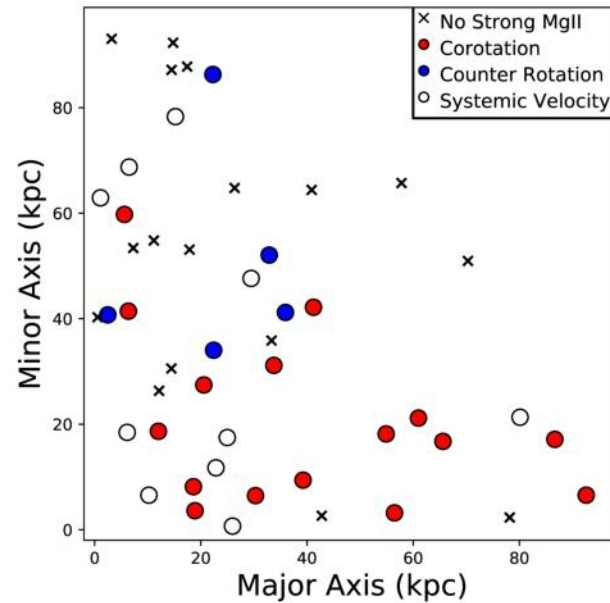


Figure 7. *Top:* Doppler shifts of Mg II systems in quasar sightlines. The location of each sightline is plotted relative to the projected plane of the galactic disk on the sky. The redshifted side of the major axis has been aligned with the positive x-axis of the coordinate system. The colorbar describes corotation (red), counter rotation (blue), and systemic absorption (white). Sightlines without Mg II detections are marked with an 'x'.

Ширины и эквивалентные ширины

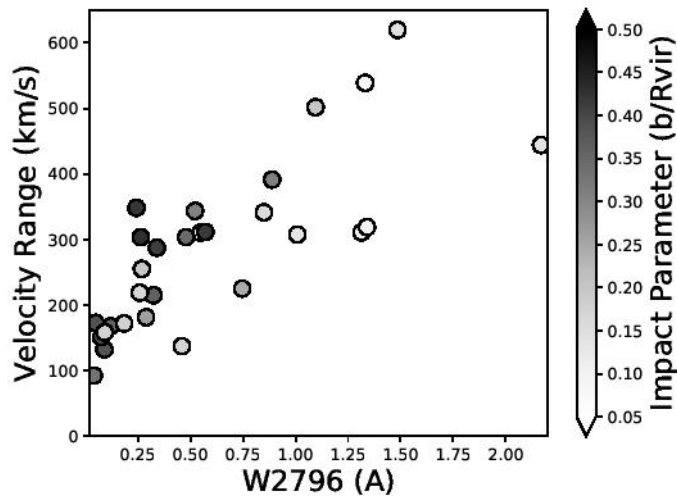


Figure 10. Velocity range of Mg II absorption versus rest-frame equivalent width of Mg II 2796. The grayscale identifies the impact parameter of each sightline. The Spearman rank-order correlation coefficient is $r_s = 0.82$ (4.3σ), indicating a significant correlation.

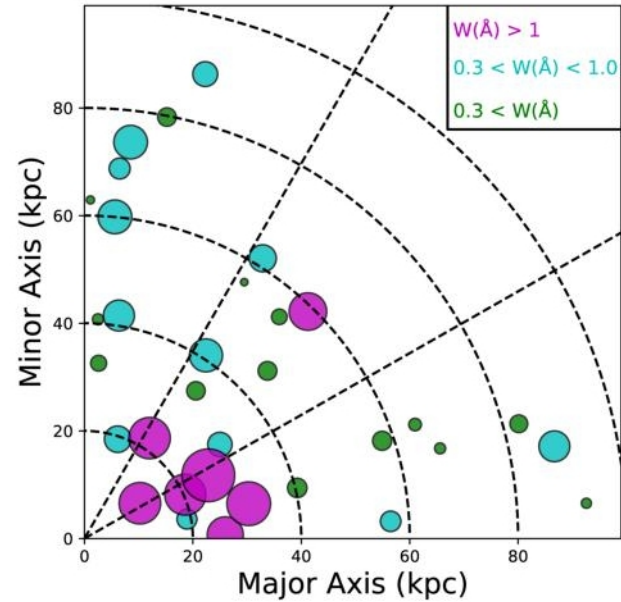


Figure 12. Absorption strength vs. azimuthal angle. We have scaled the symbol size by the equivalent width, illustrating the very strong absorbers ($W_r \geq 1.0 \text{ \AA}$), strong absorbers ($0.3 \leq W_r < 1.0 \text{ \AA}$), and optically thin absorbers ($W_r < 0.3 \text{ \AA}$). Many of the very strong absorbers were found in low impact parameter sightlines near the major axis, so they may intersect extended disks. The strong absorbers confirm the established trend that absorption strength increases near the

Модель: вращение + ветер

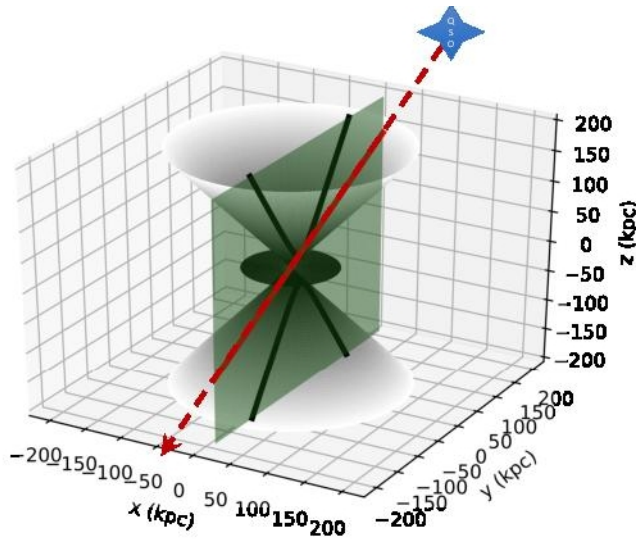


Figure 16. Coordinate system describing the three-dimensional geometry of a galactic disk and bipolar outflow. The outflow is radial in a cone perpendicular to the disk. Clouds of low-ionization gas could populate the interior of the cone or be concentrated along its surface. The angular momentum vector of the disk defines the direction of the z -axis. The angle between the z -axis and the cone defines the *outflow opening angle*, θ_{max} . The positive x -axis corresponds to the receding side of the major axis. A quasar sightline lies in a plane at $x = x_0$. The intersection of this plane with the outflow cone defines a parabola. The observer lies at a

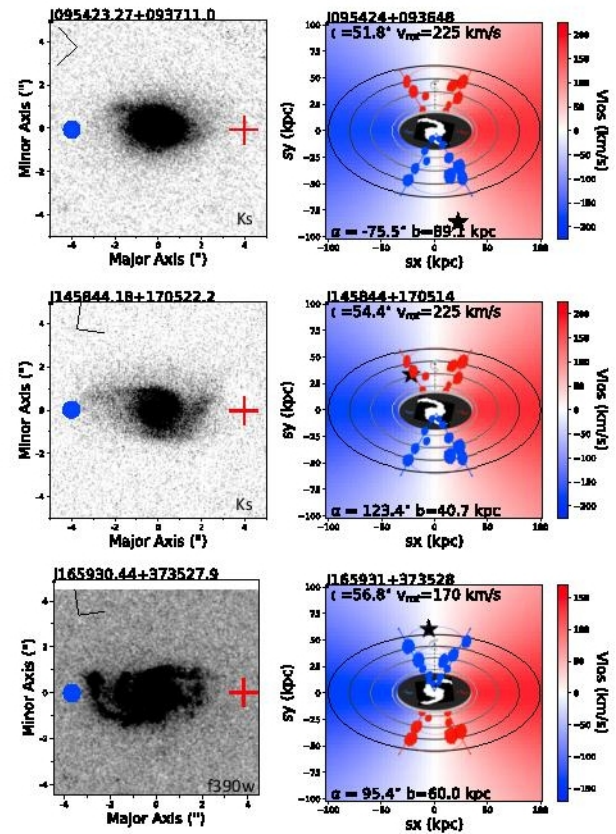


Figure 18. Examples of galaxies oriented in ways that produce outflow and disk plane components which can be easily

ArXiv:1901.11182

New Constraints on Models for Circumgalactic Gas Inflow: How Do Galaxies Get Their Gas at Low Redshi

STEPHANIE H. HO¹ AND CRYSTAL L. MARTIN¹

¹*Department of Physics, University of California, Santa Barbara, CA 93106, USA*

ABSTRACT

We constrain gas inflow speeds in several star-forming galaxies having color gradients consistent with inside-out disk growth. Our method combines new measurements of disk orientation with previously described circumgalactic absorption in background quasar spectra. Two quantities, a position angle and an axis ratio, describe the projected shape of each galactic disk on the sky, leaving an ambiguity about which side of the minor axis is tipped toward the observer. This degeneracy regarding the 3D orientation of disks has compromised previous efforts to measure gas inflow speeds. We present HST and Keck/LGSAO imaging that resolves spiral structure in redshift $z \approx 0.2$ galaxies. We then determine the sign of the disk inclination, under the assumption that the spiral arms trail the rotation. Using the measured rotation curve, we then model the projection of both radial infall in the disk plane and circular orbits onto each quasar sightline. We compare the resulting line-of-sight velocities to the observed velocity range of Mg II absorption in quasar spectra. We find maximum radial inflow speeds of 30-40 km s⁻¹ in two sightlines. We also rule out a velocity component from radial inflow in one sightline, suggesting that the structures feeding gas to these disks do not have unity covering factor (even within 30° of the major axis and low impact parameters). We recommend appropriate selection criteria for building larger samples of galaxy – quasar pairs that produce orientations sensitive to constraining inflow properties.

Выборка (на самом деле, 4 пары)

Table 2. Target Information and Summary of Spectroscopic Measurements

Quasar Name	Galaxy Name	i	θ	α	z_{gal}	b	W_r^{2796}	$v_D^{\text{Mg II}}$	Δv_{2796}	Δv_{2796}^{intr}	v_{rot}
(1)	(2)	(°)	(")	(°)	(6)	(kpc)	(Å)	(km s ⁻¹)	(km s ⁻¹)	(km s ⁻¹)	(km s ⁻¹)
J091954+291408	J091954+291345	73	23.1	15	0.23288	88	$0.52_{-0.02}^{+0.02}$	137 ± 4	[−51, 292]	[7, 235]	250
							$0.22_{-0.01}^{+0.01}$	-154 ± 9	[−266, −8]	[−208, −66]	^a
J102907+421752	J102907+421737	50	15.4	19	0.26238	65	$0.12_{-0.03}^{+0.03}$	-53 ± 15	[−134, 34]	[−76, −24]	155
J123049+071036	J123049+071050	38	17.7	4	0.39946	98	$0.08_{-0.01}^{+0.02}$	-91 ± 34^b	[−172, −21]	[−115, −79]	190
J124601+173156	J124601+173152	63	4.5	11	0.26897	19	$0.31_{-0.03}^{+0.03}$	-299 ± 11	[−404, −200]	[−314, −290]	60
J142501+382100	J142459+382113	61	23.2	8	0.21295	83	$0.24_{-0.02}^{+0.03}$	9 ± 7	[−128, 221]	[−37, 130]	190

^aWe attribute this blue, weak absorption component to a red galaxy within the group. See Paper I or Section 3 for details.

^bThe absorption system falls in a part of the LRIS spectrum without arclamp lines. Extrapolation of the dispersion solution adds an additional error term of 34 km s⁻¹ on top of the measurement error.

NOTE— (1) Name of the quasar. (2) Name of the galaxy. (3) Inclination of the galactic disk. (4) Angular separation between the galaxy and the quasar. (5) Azimuthal angle, the angle between the galaxy major axis and the quasar sightline. (6) Galaxy systemic redshift measured from emission lines. (7) Sightline impact parameter. (8) Rest-frame equivalent width of Mg II λ 2796. (9) Mg II Doppler shift measured from line profile fitting. (10) Measured velocity range. (11) Intrinsic velocity range (corrected for the line broadening effect due to the instrumental resolution). (12) Asymptotic galaxy rotation speed.

Две пары, где все хорошо

10

HO & MARTIN

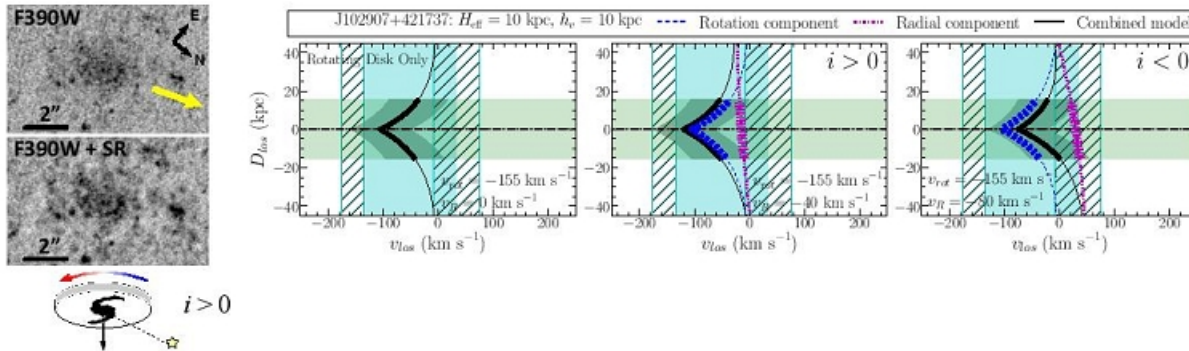


Figure 7. J102907+421737: Disk tilt helps tighten constraint on radial inflow speed. The spiral arms become prominent after processing the WFC3 F390W image as shown in Figure 2. The yellow arrow points to the quasar sightline position. The schematic disk diagram illustrates the wrapping direction of the spiral arms, the sense of disk rotation, and the deduced sign of disk inclination. A rotating disk (left) can produce absorption that marginally matches the observed LOS velocity range within measurement uncertainties. Disks with positive (middle) and negative (right) inclination allow maximum radial inflow speeds of 40 km s^{-1} and 80 km s^{-1} respectively. Otherwise, the absorption becomes too blue or not blue enough at the disk midplane. With the inferred disk inclination being positive, the radial inflow speed cannot exceed 40 km s^{-1} .

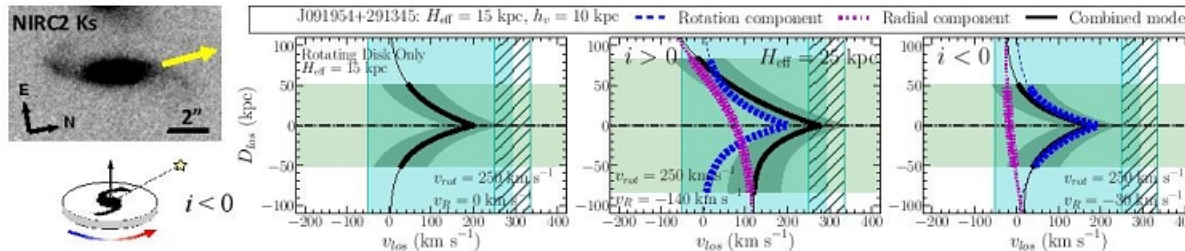


Figure 8. J091954+291345: Disk tilt helps tighten constraint on radial inflow speed. The K_s galaxy image clearly shows the spiral arms. Together with the disk rotation, we deduce the disk as negatively inclined (see the schematic diagram). A rotating disk marginally reproduces the LOS velocity range of the absorption (left). Disks with positive (middle) and negative (right) inclination allow maximum radial inflow speeds of 140 km s^{-1} and 30 km s^{-1} respectively. Hence, deducing the disk as negatively inclined limits the inflow speed to 30 km s^{-1} .

H_{eff} of 10 kpc and an exceptionally high radial inflow speed of 480 km s^{-1} . However, the disk is positively inclined. A rotating disk already produces bluer absorp-

the radial inflow speeds permitted by the model largely overlap. Therefore, knowing the disk tilt cannot tighten the constraint on the inflow speed.

А тут плохо!

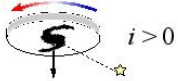
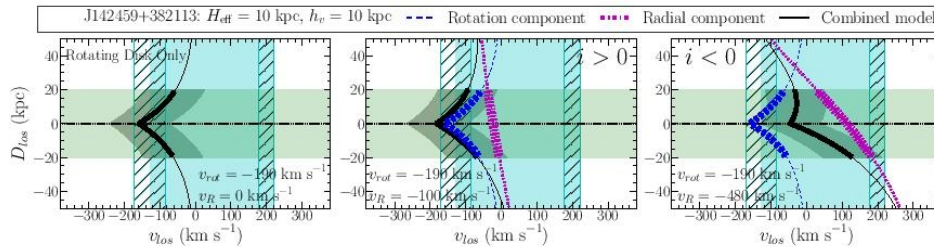
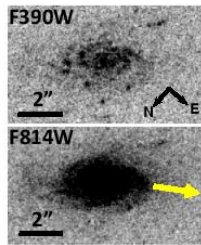


Figure 9. J142459+382113: Disk tilt excludes radial inflow detection. Both WFC3 F390W and F814W images show the spiral arms. Disk rotation alone (left) cannot reproduce the broad absorption that spans both sides of the galaxy systemic velocity and the rotation produces bluer absorption at the disk midplane than measured. Only a negatively inclined disk (right) can reproduce the LOS velocity range. However, the disk is positively inclined (see the schematic diagram). Introducing radial inflow produces even bluer net absorption (middle) than a rotating disk (left) at the midplane. We demonstrate this problem using a fiducial inflow speed of 100 km s^{-1} . Hence, the positively inclined disk of this galaxy excludes the detection of radial inflow in the sightline.

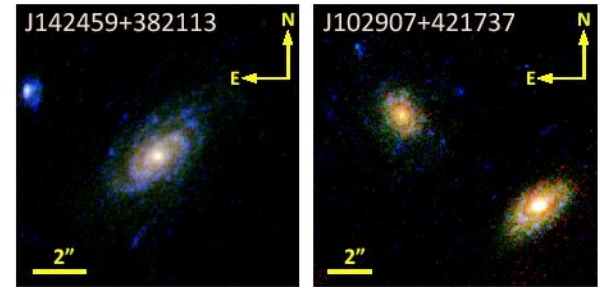


Figure 11. Three-color images of two disk galaxies. The color images are created by combining images in the WFC3 F390W (blue), WFC3 F814W (green), and NIRC2 K_s (red) bands. For J102907+421737, our target galaxy ($z=0.26238$) is on the left, and the galaxy on the right ($z=0.18469$) does not form a group with our galaxy. The disks of both J142459+382113 and J102907+421737 are more extended in bluer bands, which imply each outer disk has a younger stellar population and a lower metallicity.

ArXiv: 1901.11416

MusE GAs FLOW and Wind (MEGAFLOW) II. A study of gas accretion around $z \approx 1$ star-forming galaxies with background quasars [★]

Johannes Zabl,^{1,2†} Nicolas F. Bouché,^{1,2} Ilane Schroetter,^{3,1} Martin Wendt,^{4,5}
Hayley Finley,^{6,1} Joop Schaye,⁷ Simon Conseil,² Thierry Contini,¹ Raffaella A. Marino,⁸
Peter Mitchell,² Sowgat Muzahid,⁷ Gabriele Pezzulli,⁸ Lutz Wisotzki⁵

¹ *Institut de Recherche en Astrophysique et Planétologie (IRAP), Université de Toulouse, CNRS, UPS, F-31400 Toulouse, France*

² *Univ Lyon, Univ Lyon1, Ens de Lyon, CNRS, Centre de Recherche Astrophysique de Lyon UMR5574, F-69230 Saint-Genis-Laval, France*

³ *GEPI, Observatoire de Paris, CNRS-UMR8111, PSL Research University, Univ. Paris Diderot, 5 place Jules Janssen, 92195 Meudon, France*

⁴ *Institut für Physik und Astronomie, Universität Potsdam, Karl-Liebknecht-Str. 24/25, 14476 Golm, Germany*

⁵ *Leibniz-Institut für Astrophysik Potsdam (AIP), An der Sternwarte 16, 14482 Potsdam, Germany*

⁶ *Stockholm University, Department of Astronomy and Oskar Klein Centre for Cosmoparticle Physics, AlbaNova, University Centre SE-10691, Stockholm, Sweden*

⁷ *Leiden Observatory, Leiden University, PO Box 9513, NL-2300 RA Leiden, the Netherlands*

⁸ *Department of Physics, ETH Zürich, Wolfgang-Pauli-Strasse 27, 8093 Zürich, Switzerland*

9 nap!

Выборка

Field and absorber	Galaxy ID (1)	Coordinate (2)	b (3)	Δv (4)	$f_{[\text{OII}]}$ (5)	Note
Field: J0103p1332 $z_{\text{abs}} = 0.788$	gal_0788_3_25	01:03:32.37 +13:32:36.1	20	61	7.2 ± 0.1	
Field: J0145p1056 $z_{\text{abs}} = 0.554$	gal_0554_3_52	01:45:13.28 +10:56:28.8	22	-97	3.2 ± 0.1	
Field: J0800p1849 $z_{\text{abs}} = 0.608$	gal_0608_10_108	08:00:05.20 +18:49:32.6	65	-12	26.0 ± 1.0	a
	gal_608_19_140	08:00:05.41 +18:49:20.5	129	-419	–	b
	gal_608_23_163	08:00:05.03 +18:49:13.1	155	-278	1.06 ± 0.04	
	gal_608_27_322	08:00:03.37 +18:49:56.6	184	-60	0.5 ± 0.1	
	gal_608_30_144	08:00:05.79 +18:49:10.9	201	6	0.7 ± 0.1	
Field: J1039p0714 $z_{\text{abs}} = 0.949$	gal_0949_6_324	10:39:36.42 +07:14:32.4	49	141	9.5 ± 0.1	
	gal_0949_9_344	10:39:36.48 +07:14:36.1	72	111	3.1 ± 0.1	c
Field: J1107p1021 $z_{\text{abs}} = 1.048$	gal_1048_5_359	11:07:42.71 +10:21:31.4	41	-45	3.8 ± 0.1	
Field: J1236p0725 $z_{\text{abs}} = 0.912$	gal_0912_2_246	12:36:24.25 +07:25:50.8	17	34	8.7 ± 0.6	
Field: J1358p1145 $z_{\text{abs}} = 1.418$	gal_1418_3_291	13:58:09.26 +11:45:59.2	30	-60	14.8 ± 0.1	d
	gal_1418_5_238	13:58:09.22 +11:45:55.1	40	-186	1.4 ± 0.1	
Field: J1509p1506 $z_{\text{abs}} = 1.046$	gal_1046_2_351	15:09:00.10 +15:06:36.5	13	68	5.4 ± 0.2	
Field: J2152p0625 $z_{\text{abs}} = 1.053$	gal_1053_6_57	21:52:00.36 +06:25:19.7	49	-68	11.4 ± 0.3	
	gal_1053_23_341	21:51:59.54 +06:25:38.4	187	6	5.7 ± 0.2	

Table 3. Absorber-galaxy identification. Primary galaxies are indicated in bold. (1) ID. The first number in the ID indicates the absorber redshift, the second the impact parameter in arcsec, and the third the position angle between quasar and galaxy in degrees. (2) Right ascension and Declination of galaxy (hh:mm:ss dd:mm:ss; J2000); (3) Impact parameter [kpc]; (4) Velocity offset between absorber redshift, z_{abs} , and redshift of galaxy, z_{gal} [km s^{-1}]; (5) [OII] flux in units of $10^{-17} \text{ erg s}^{-1} \text{ cm}^{-2}$ as obtained from the 1D line flux (fluxes are measured in large *SExtractor MAG_AUTO* apertures, but not aperture corrected).

Note. a) blend w. foreground galaxy; b) passive HK; c) aligned with minor axis to quasar; d) At this redshift Ca H&K falls outside of the MUSE wavelength range and our automatic detection would miss quiescent galaxies without any residual [OII] line emission. As an alternative, we checked here for stellar MgII $\lambda 2796, 2803$ absorption, but did not find any additional candidates.

Выборка

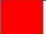








	ID	$E_{\text{Mass}}(B - V)$	$E_{\text{SED}}(B - V)$	$\text{SFR}_{[\text{OII}];2}$	$\text{SFR}_{[\text{OII}];3}$	SFR_{SED}	M_*	$\delta(MS)$	S05	B
	(1)	(2)	(3)	(4)	(5)	(6)	(7)	(8)	(9)	(10)
	J0103p1332	$0.22^{+0.09}_{-0.12}$	$0.00^{+0.68}_{-0.00}$	$3.1^{+0.7}_{-0.9}$	$0.9^{+1.5}_{-0.0}$	$0.8^{+26.7}_{-0.0}$	$9.8^{+0.0}_{-0.4}$	$0.18^{+0.52}_{-0.11}$	55 ± 6	-19.6
	J0145p1056	$0.23^{+0.10}_{-0.09}$	$0.26^{+0.29}_{-0.09}$	0.8 ± 0.2	$0.9^{+0.6}_{-0.2}$	$1.5^{+4.3}_{-0.5}$	$9.8^{+0.3}_{-0.1}$	$-0.35^{+0.17}_{-0.19}$	117 ± 27	-19.2
	J0800p1849	0.18 ± 0.09	$0.09^{+0.20}_{-0.01}$	4.6 ± 1.0	$2.7^{+1.3}_{-0.1}$	$1.4^{+3.0}_{-0.0}$	$9.5^{+0.2}_{-0.0}$	$0.60^{+0.12}_{-0.16}$	83 ± 7	-20.0
	J1039p0714	0.21 ± 0.09	$0.77^{+0.04}_{-0.10}$	5.5 ± 1.2	$112.3^{+9.3}_{-26.9}$	$110.2^{+20.1}_{-53.2}$	$9.7^{+0.1}_{-0.0}$	$0.41^{+0.12}_{-0.14}$	120 ± 11	-20.6
	J1107p1021	$0.28^{+0.12}_{-0.10}$	$0.26^{+0.18}_{-0.03}$	$4.9^{+1.4}_{-1.1}$	$4.3^{+1.8}_{-0.3}$	$6.5^{+9.5}_{-1.0}$	$10.0^{+0.3}_{-0.1}$	$0.06^{+0.26}_{-0.21}$	134 ± 14	-20.6
	J1236p0725	$0.39^{+0.18}_{-0.09}$	$0.64^{+0.70}_{-0.00}$	$12.8^{+5.4}_{-2.7}$	$48.8^{+79.8}_{-0.5}$	$7.1^{+680.4}_{-0.0}$	$10.5^{+0.5}_{-0.0}$	$0.14^{+0.15}_{-0.24}$	164 ± 17	-20.8
	J1358p1145	$0.26^{+0.12}_{-0.11}$	$0.26^{+0.10}_{-0.07}$	$29.9^{+8.2}_{-7.7}$	$28.9^{+6.5}_{-4.6}$	$27.8^{+44.9}_{-4.6}$	9.9 ± 0.3	$0.78^{+0.39}_{-0.22}$	48 ± 1	-22.0
	J1509p1506	0.14 ± 0.09	$0.60^{+0.05}_{-0.12}$	3.7 ± 0.8	$43.2^{+5.5}_{-12.1}$	$38.6^{+14.9}_{-18.9}$	$9.3^{+0.2}_{-0.1}$	$0.51^{+0.15}_{-0.17}$	95 ± 12	-20.2
	J2152p0625	$0.34^{+0.12}_{-0.10}$	$0.43^{+0.15}_{-0.14}$	$16.8^{+4.8}_{-3.8}$	$27.3^{+9.6}_{-8.9}$	$22.1^{+28.6}_{-11.0}$	$10.2^{+0.3}_{-0.1}$	$0.39^{+0.23}_{-0.21}$	125 ± 13	-21.2

Table 5. Physical parameters of the galaxies as obtained from the [OII] emission line fluxes and SED fitting. (2) Nebular $E(B - V)$ estimated from stellar mass (Eq. (1)); (3) nebular $E(B - V)$ as obtained from SED fitting (see §5.2); (4) [OII] based SFR [$M_{\odot} \text{ yr}^{-1}$] from Eq. (2) and assuming $E_{\text{Mass}}(B - V)$ as extinction; (5) Same as in 4, but using $E_{\text{SED}}(B - V)$ as extinction estimate; (6) Instantaneous SFR [$M_{\odot} \text{ yr}^{-1}$] directly from SED fit; (7) Stellar mass [$\log_{10}(M_{\odot})$] from SED fit; (8) Distance from the Main Sequence ($\log(\text{sSFR}(\text{Obs})/\text{sSFR}(\text{MS}))$). The observed sSFR was calculated using columns 4) and 7); (9) $S_{0.5} = (0.5v_{\text{max}}^2 + \sigma_0^2)^{0.5}$ [km s^{-1}] (10) rest-frame B absolute magnitude calculated from best fit-SED model [mag].

Сразу модель!

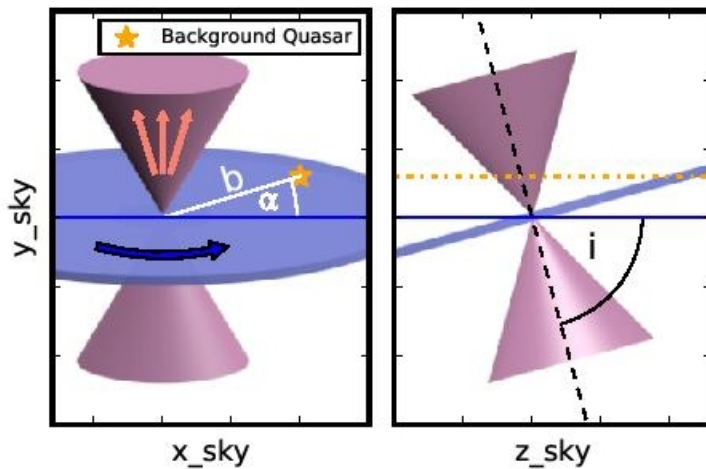


Figure 1. Assumed geometry of the cold CGM. **Left:** CGM geometry as observed on the sky-plane, where x_{sky} is without loss of generality aligned with the disk's projected major axis. The impact parameter b and the azimuthal angle α are the polar coordinates of the background quasar (orange) on the sky-plane. **Right:** Same geometry as seen from the side, where z_{sky} is along the line-of-sight. i is the inclination of the disk on the sky.

(iv) The primary galaxy is not a clear merger and does not have strong AGN signatures.

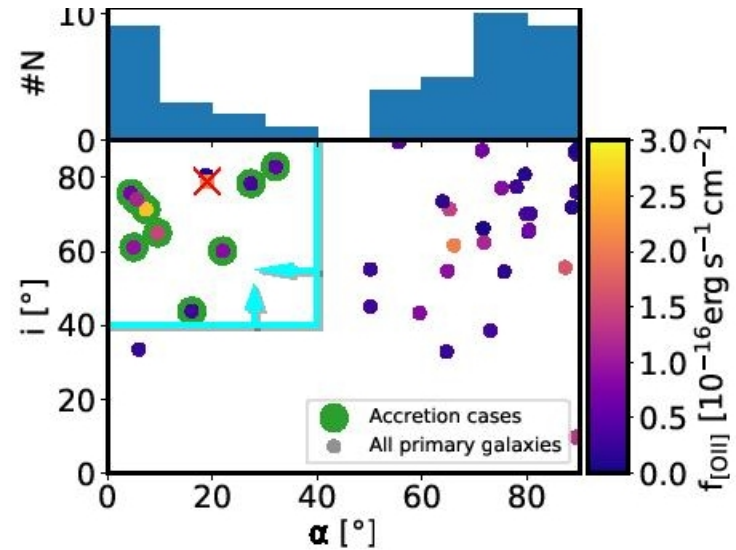


Figure 2. Distribution of the MEGAFLOW primary MgII host galaxies (see §4.2). In the upper part the α histogram is shown for the points in the $\alpha - i$ plane below. The colour-scale indicates the [OII] flux of the galaxies. The nine points circled in green within the cyan boundaries are suitable (as in §4.3) candidates for this study. One galaxy in the selection region is excluded as it is an AGN (red cross). Two of the 45 primary galaxies are omitted in the α histogram, as we could not obtain robust α for those. Four further primary galaxies are not included in the lower panel, as we could not obtain robust inclinations.

Распределение

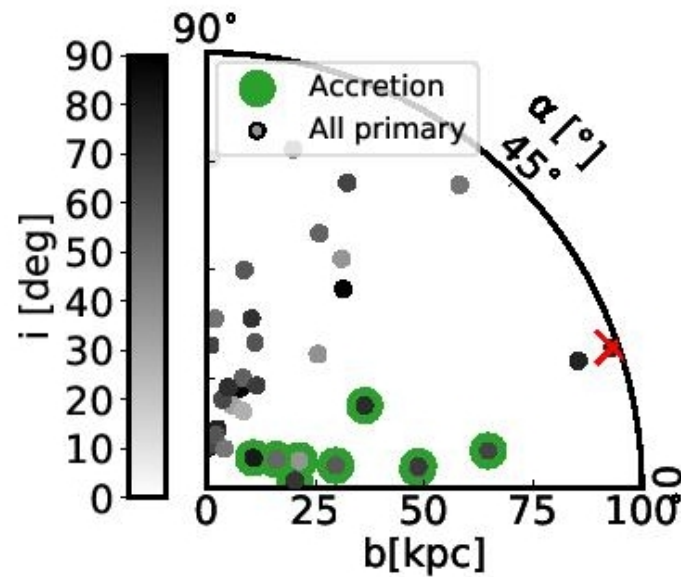
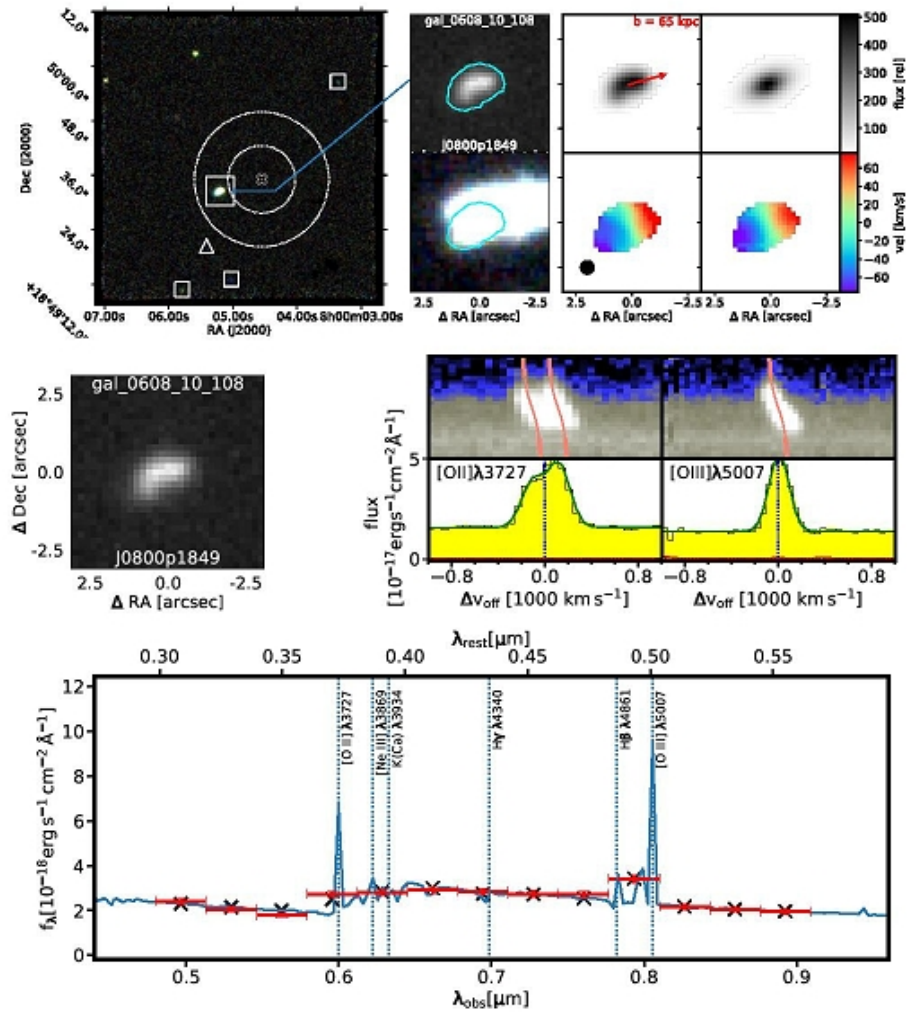
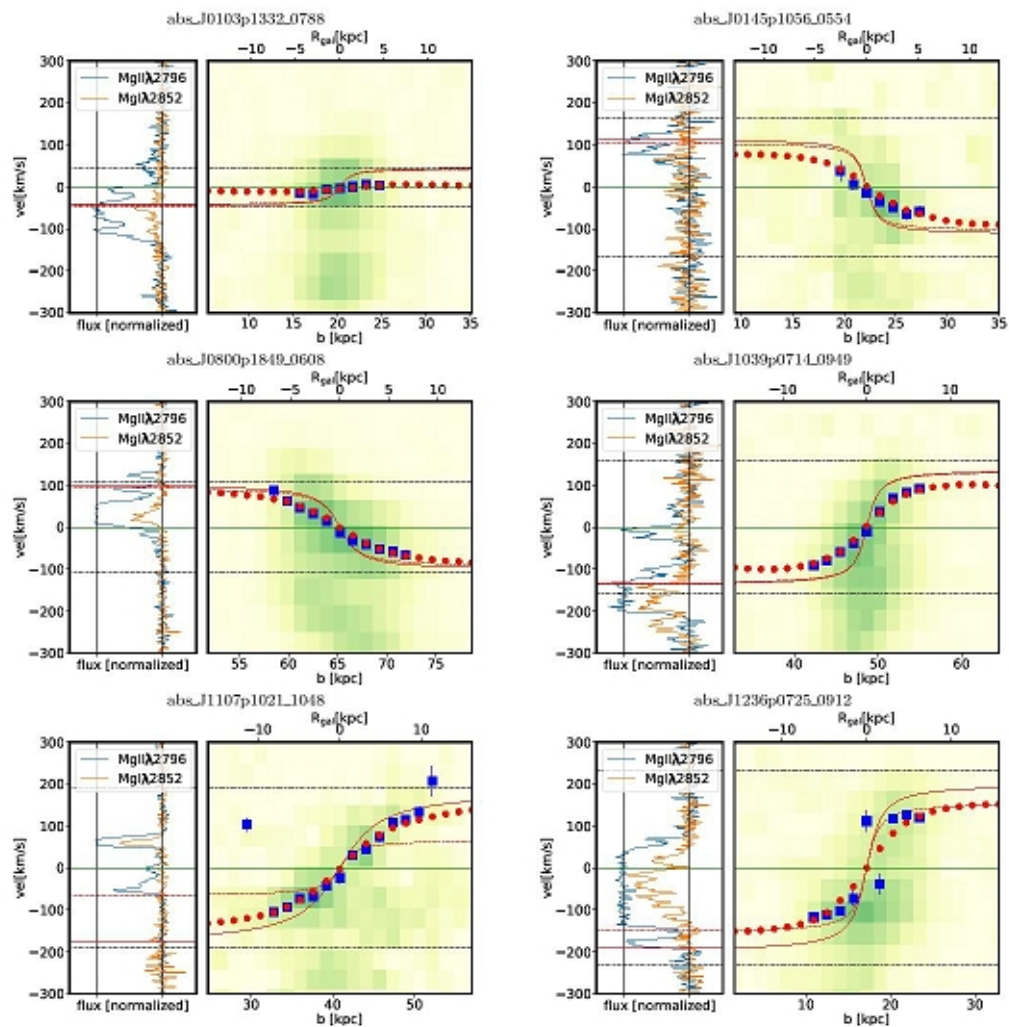


Figure 3. Same galaxies as in Fig. 2, but here shown in the impact parameter vs α diagram. The grey-scale indicates here the inclination. The two objects at $b \approx 50$ kpc are overlapping. For an explanation of the red cross see Fig. 2.

Пример анализа



А так делается вывод о ко-ротации



Сводка по всем 9 парам

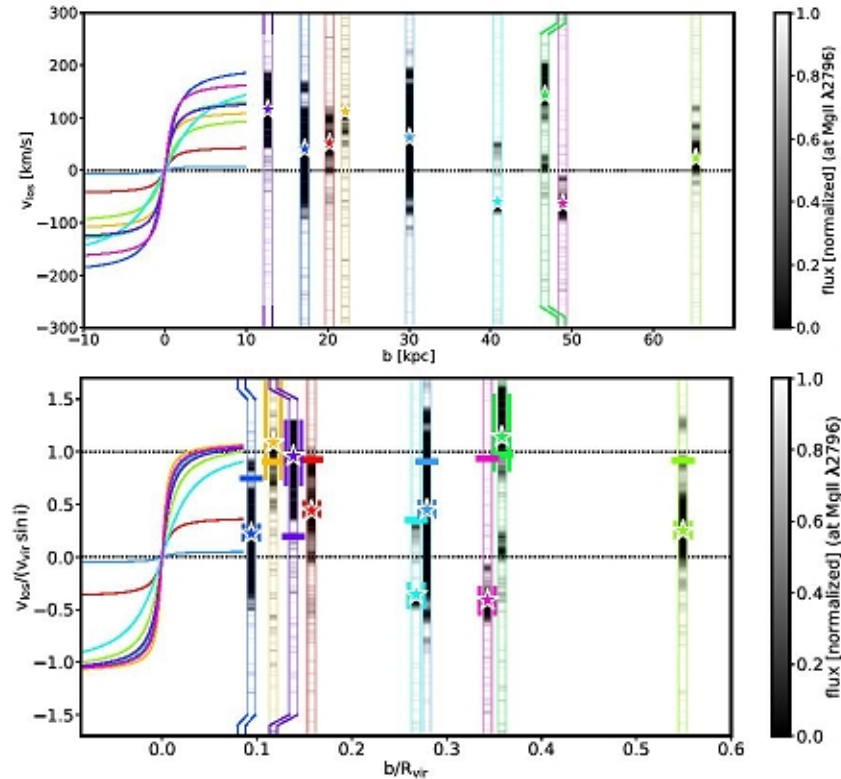


Figure 7. Mg II $\lambda 2796$ absorption compared to galaxy rotation for each of the nine galaxies-absorber pairs of this study. Galaxy-absorber pairs can be identified by matching colours (as in Table 4). The grey vertical bars represent the Mg II $\lambda 2796$ profile where the darker regions indicate more absorption, and shifted in the x-direction when they would overlap. The stars indicate the peak of the Mg II profile (see §5.5). The solid lines represent the rotation curves (at the observed inclination), as obtained from the GalPaK^{3D} [O II] fits, and measured along the galaxy major axis. The top panel shows the kinematics as a function of impact parameter b , not galactocentric distance. The bottom panel shows the same as in the upper panel, but here b and v_{obs} have been normalized by r_{vir} and $v_{\text{vir}} \sin i$, respectively. The coloured bold vertical bars indicate the impact of the uncertainties for $v_{\text{vir}} \sin i$ on the normalized peak absorption velocity. The coloured horizontal bars indicate the velocity expected from extrapolating the rotating galaxy disk out to the galactocentric radius of the quasar sight-line assuming a thin disk and rotation with v_{vir} .

Но профили широкие!

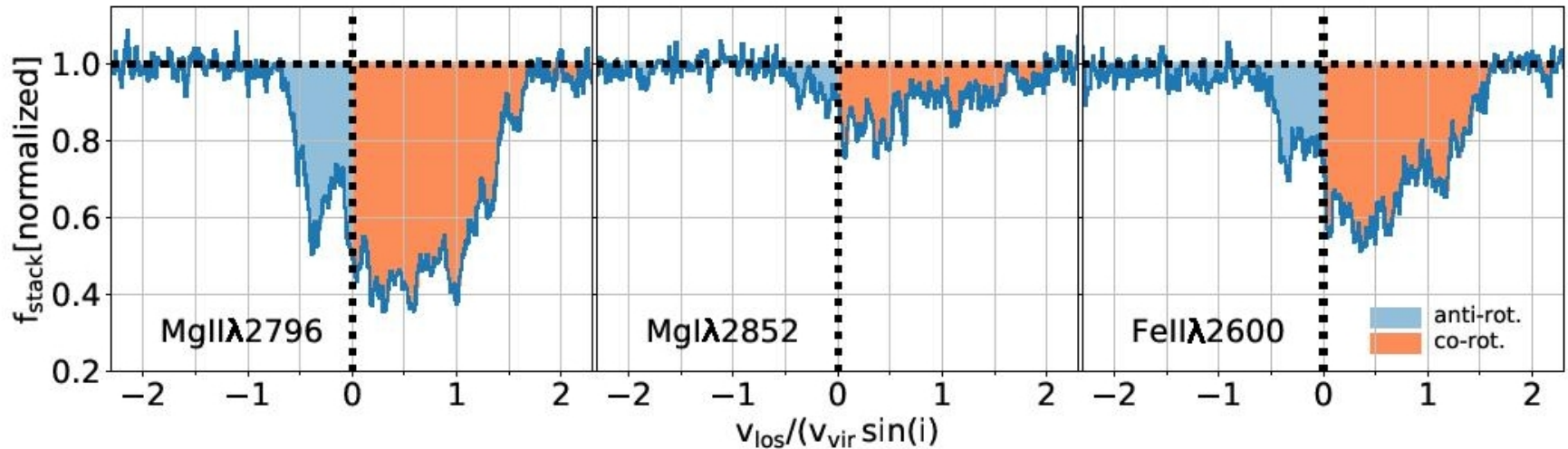


Figure 8. Average absorption profile for our sample of nine galaxy-absorber pairs. The MgII stack was obtained by calculating the mean of the profiles shown in the lower panel of Fig. 7. The stacks for MgI and FeII were obtained in an identical way. As in Fig. 7, for those pairs where the galaxy-rotation was blue-shifted towards the quasar sight-line, we flipped both galaxy and absorber velocities. Consequently, all co-rotation has positive velocities in these stacks (salmon), while all counter-rotating gas has negative velocities (light-blue).

Согласуется с предсказаниями радиального втекания газа

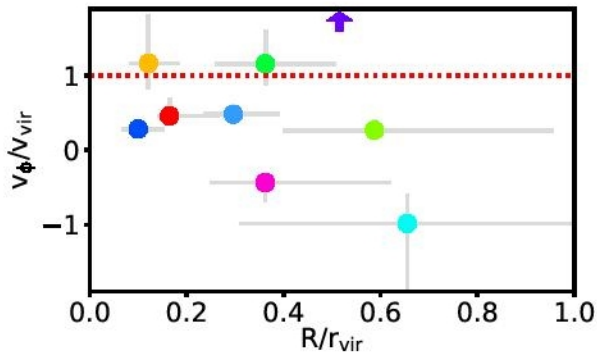


Figure 9. Tangential velocity v_ϕ inferred from v_{los} under the assumption that the gas is on pure circular orbits in the disk plane. For gas on stable circular orbits the expectation is that $v_\phi \approx v_{\text{vir}}$. The two cases at the extreme ends of the v_ϕ/v_{vir} distribution (*J1107* cyan; *J1509* purple, indicated by an arrow as outside of plot range) have both the highest α 's and inclinations among our nine galaxy-absorber pairs. The values of the plotted points are listed in Table C4 of the Supplementary Appendix.

6.3 Disk with angular and radial motion - Cold accretion disks

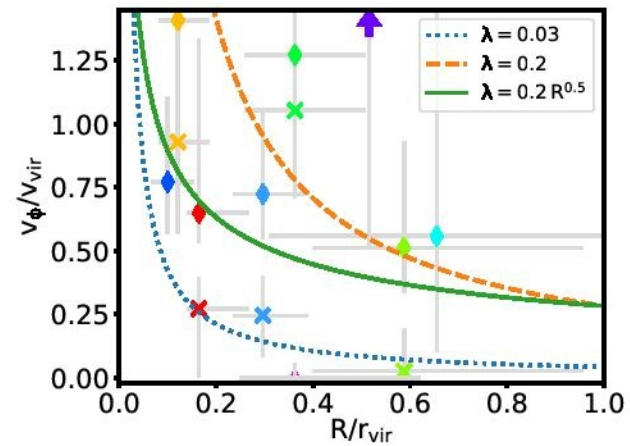


Figure 10. Rotation velocities, v_ϕ , inferred from measured v_{los} under the assumption of a radial velocity component with $v_r = -0.6v_{\text{vir}}$ and co-rotation with the galaxy for each of the nine absorbers. There can be up to two solutions per absorber. The projected LOS components of v_r and v_ϕ have the same sign for solutions indicated by stars, while they have opposite signs for solutions indicated by diamonds. The lines indicate different spin parameters (λ , see Eq. (12)), with their values indicated in the legend. The values of the plotted points are listed in Table C4 of

... достаточного, чтобы питать SF

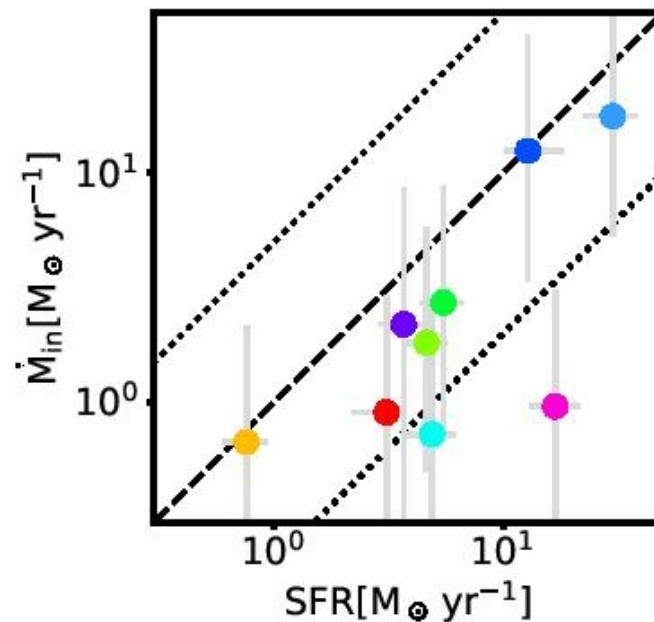


Figure 11. Mass inflow rate estimated from MgII equivalent width plotted against SFR estimate obtained from [O II] flux corrected for reddening using the $E(B - V)$ estimate based on the Garn & Best (2010) M_* -extinction relation. The dashed line represents a 1:1 relation. The dotted lines represent deviations from the 1:1 correspondence by a factor five.